European Journal of Mechanics / A Solids 108 (2024) 105417

Contents lists available at ScienceDirect

European Journal of Mechanics / A Solids

journal homepage: www.elsevier.com/locate/ejmsol

Full Length Article

Crystal-plasticity modelling of the yield surfaces and anelasticity in the elastoplastic transition of metals

Arash Imani Aria, Bjørn Holmedal, Tomáš Mánik, Knut Marthinsen *

Department of Materials Science and Engineering, Norwegian University of Science and Technology, NO-7491, Trondheim, Norway

ARTICLE INFO

Keywords:
Full-field crystal-plasticity
10με offset yield surfaces with pointed vertexes
Elastoplastic transition of pre-strained polycrystal metals

ABSTRACT

The paper presents a full-field crystal-plasticity computational investigation of $10\mu\varepsilon$ small-strain-offset yield surfaces with pointed vertexes that are seen in the elastoplastic transition of pre-strained polycrystal metals. It is concluded that the shape of these yield surfaces obtained with a full-field spectral solver compares reasonably well with calculated ones by a simple aggregate Taylor model. The influence of material strength, work hardening, and texture are discussed. An assessment is made of the origin of anelasticity and Bauschinger effects at small strains, considering two mechanisms. Firstly, there is a built-in composite effect in crystal elastoplastic simulations due to the mixture of elastically and plastically loaded grains. Secondly, kinematic hardening of reverse slip systems will contribute to the Bauschinger effect. Based on analyses of the computed selected cases and comparison to previously published measurements, it is concluded that both mechanisms are important.

1. Introduction

During the elastoplastic transition, a fraction of the grains deforms plastically while the rest are elastically loaded. In the classical continuum-plasticity modelling, with a flow rule, the elastoplastic transition is modelled to occur where all grains have started to deform plastically. Pragmatically, when measuring the yield stress, e.g., from a tensile test, the yield stress is taken as the stress at a certain plastic strain during monotonic loading in that stress direction. However, in some grains, plasticity starts at significantly lower stress, and an increasing fraction of the grains gradually reaches the limit for the onset of dislocation glide, i.e., plastic flow. Hence, the yield locus depends on the magnitude of the probing strain.

The literature on calculations of texture effects on the conventional yield surface obtained with a probing strain of $\approx 0.2\%$ by full-field crystal plasticity modelling, is extensive, see e.g., (Aria et al., 2023; Han et al., 2020; Liu and Pang, 2021; Zhang et al., 2019). However, spatially resolved calculations of the instant yield surface after a pre-strain, using a small probing strain of $\approx 10^{-3}\%$, has not been reported earlier. Experimental works on measuring the yield loci after pre-deformation, in the early part of the elastoplastic transition, started in the 1950s. Motivated by the interest in the initial stress and work-hardening anisotropy and for the Bauschinger effect, Naghdi and Rowley (1954) performed experiments on thin-walled, tubular specimens, measuring the yield locus at very small plastic strains. Based on their experimental results, they found that this yield locus was convex but with initial stress and work-hardening anisotropy. Furthermore, their measurements strongly suggested the existence of a pointed vertex in the loading direction. This pointed vertex only appeared when probing yielding at very small strains. The tip of the pointed vertex would point approximately onto the conventional yield surface, typically measured at 0.2% plastic strain. Many similar experiments were performed in the following years, with torsion, tension, compression, and the inner pressure of thin-walled tubes, e.g. (Phillips and Lee, 1979) on pure commercial aluminum. With sufficiently small probing strains, all investigations reported a pronounced Bauschinger effect, but it was unclear if a pointed vertex evolved during pre-deformation. Hecker (1976) reviewed 54 experimental works in 1976 and concluded that only five reported sharp corners, sixteen reported rounded corners, while the majority did not report vertexes at all. Hecker suggested that a sharp vertex could be erased during the unloading required to measure the vertex. Later, the existence of a sharply pointed vertex was verified by Kuwabara et al. (2000), avoiding the unloading by performing an abrupt strain-path change, as suggested by Kuroda and Tvergaard (1999), see also Kuroda (2022). Whether it is a sharp or a blunt vertex may be difficult to conclude from the experimental resolution, but at least a "nose" on the yield surface is seen when being measured with small probing strains.

* Corresponding author.
E-mail address: knut.marthinsen@ntnu.no (K. Marthinsen).

https://doi.org/10.1016/j.euromechsol.2024.105417
Received 17 February 2024; Received in revised form 13 June 2024; Accepted 10 August 2024
Available online 13 August 2024

The existence of a pointed vertex is not part of the classical incremental continuum plasticity theory, where the strain-rate tensor can be derived from a stress potential (Hill, 1950). From the crystal-plasticity theory, but disregarding the elasticity, the analyses by Bishop and Hill (1951) and Koiter (1953) concluded that the result of the crystal plasticity occurring in each grain could be described by an effective yield surface of the polycrystal and associated flow, similar as in the continuum-plasticity theories. The analysis of the homogenization of the plastic Taylor model provided a direct interpretation of the Tresca yield surface, which can be derived in the limit of infinitely many slip systems (Koiter, 1953). Even though the rate-independent crystal-plasticity theory with the Schmid assumption results in faceted yield surfaces with many vertexes for each crystal (56 for fcc), the averaging of all crystals in a representative volume element (RVE) could not explain the pointed vertex observed experimentally in the loading direction.

A physical mechanism for the pointed vertex was provided by Hill (1967) and is based on the behavior of the mixture of elastically and plastically loaded grains existing during the elastoplastic loading of polycrystalline aggregates. A mathematical description of this mechanism requires elasticity to be included in the crystal plasticity theory. Calculations of pointed vertexes were then made by Hutchinson (1970) including elasticity, using the Taylor-Lin model (Lin, 1957) and a self-consistent homogenization scheme (Hill, 1965) as a simplified model for the elastoplastic crystal plasticity behavior. This provided a qualitative prediction of the phenomenon.

Based on analyzing double slip, Pan and Rice (1983) suggested a qualitative explanation why a viscoplastic model for the resolved shear stress will make the pointed vertex blunted, rather than sharp. To the authors' knowledge, a quantitative investigation of this difference and the limit of a vanishing strain rate sensitivity have not yet been published.

Interestingly, the presence of pointed vertexes can also be described by path-independent deformation theories (Batdorf, 1949) based on Hencky's theory (Hencky, 1924), where the stress depends on the total plastic strain. These theories were originally developed for dealing with nonlinear, small plastic strains occurring in the elastoplastic transition. Due to the theoretical shortcomings of the deformation theory, as pointed out by Hill (1950), i.e., not being able to deal with that the plastic deformation in most cases is path independent, these theories are not frequently used, and their validity is otherwise, in the plastic regime, limited to cases of proportional or simple loading.

The main issue with the classical incremental flow theory is that without the pointed vertex, the predictions may not correctly capture all cases of plastic buckling and plastic flow instabilities like shear-band formation or local necking (Kuroda, 2022; Yoshida and Kuroda, 2012). For example, a realistic prediction of sheet necking in biaxial tension depends sensitively to the magnitude of the introduction of an initial finite (geometrical) imperfection. The reason why the crystal-plasticity models can give a better description is the pointed vertex, which allows a rapid change of the direction of the plastic strain-rate tensor, which shortens the strain path towards the instability mode. The classical incremental plasticity flow theory with the common assumption of associated flow, on the other hand, requires the strain-rate tensor to remain normal to the outer, enveloping conventional yield surface during the sliding along the yield surface towards the new loading mode of the instability. This requires a finite significant amount of perturbation for local strain-path change toward the instability to be realized. A motivation for the current investigation of the prediction of pointed vertices by crystal plasticity models is the recent progress (Yoshida, 2017; Yoshida and Tsuchimoto, 2018; Zhang and Han, 2023; Zhang et al., 2022) in modifying the classical incremental flow theory, where the influence of the pointed vertex is modelled by phenomenological non-associated flow rules that are inspired by and calibrated to crystal plasticity simulations.

In crystal plasticity modelling, the sharply pointed vertex is a consequence of sharp corners of the single crystal yield surface when it, in the rate-independent case, obeys the Schmid condition with a critical resolved shear stress for each slip system. However, a strain rate-dependent model will predict an increasingly rounded pointed vertex with increased strain-rate sensitivity. With a rounded corner of increasing sharpness, the required amount of perturbation decreases, and with a sharp vertex, the instabilities become infinitesimal (Yoshida and Kuroda, 2012). The main problem with using the flow theory and adding some imperfections is the sensitivity to the magnitude of the small imperfections required to predict the instabilities.

Modified versions of the path-independent deformation theories can predict biaxial necking, plastic buckling, shear-band formation, and related instabilities without finite disturbances by applying the so-called corner theories (Christoffersen and Hutchinson, 1979; Gotoh, 1985; Storen and Rice, 1975). However, the justification and applicability of these models are questionable for more general strain paths (Kuroda, 2022). The instabilities can, however, also be predicted by modifications of the flow theory, where the associated flow condition, i.e., the requirement that the plastic strain increment is always normal to the yield surface, is relaxed (Kuroda and Tvergaard, 2001a, 2001b; Simo, 1987; Yoshida, 2017). These approaches are promising, but further testing and development of the modelling of the plastic strain increment are still required. Complementary to challenging experimental testing of complex strain paths, virtual tests by crystal-plasticity simulations provide valuable data, insight, and understanding of the behaviour to be modelled, provided the crystal plasticity models grasp the essence of the mechanisms involved.

An important aspect of the subsequent yield surfaces measured at small-probing strains is the strong Bauschinger effect they reveal, compressing the yield surface in the reverse direction of the loading. Using an aggregate crystal-plasticity model, which included elasticity, Hutchinson (1970) showed clearly that the Bauschinger effect could be qualitatively captured as a composite effect of the coexisting elastically and plastically loaded grains. Toth et al. (2000) argue that the Taylor-Lin model (Lin, 1957) can qualitatively capture the Bauschinger effect. A few works report quantitative agreement between crystal plasticity simulations and experiments based on this mechanism only (Iftikhar and Khan, 2021; Iftikhar et al., 2021, 2022), while other works report the need for additional explicit models for backstress at the slip-system level (Hu et al., 2015; Lu et al., 2020).

The Bauschinger effect is important in spring-back after forming. In continuum models, it can be captured by either kinematic hardening, see, e.g., the review by Chaboche (2008), or yield-surface distortions see, e.g. (Barlat et al., 2011, 2020; Holmedal, 2019; Reyne and Barlat, 2022), combined with models for an appropriate, very fast evolution of corresponding internal variables, e.g., the backstress tensor. However, the Bauschinger effect may also lead to anelasticity, which makes predicting springback during forming operations challenging (Wagoner et al., 2013). Anelasticity is mechanically reversible and thermodynamically irreversible and is, therefore, different from both elasticity and plasticity (Li and Wagoner, 2021). The anelasticity phenomenon cannot be adequately predicted without a backstress for the critical resolved shear stress of each slip system, distinguishing forward and backward slip directions (Bong et al., 2017; Kassner et al., 2013).

The origin of the backstress at the slip-system level is that plastic strain occurring by dislocation glide is, to some extent, reversible. At the very small strain scale, probably indistinguishable from the crystal elasticity, it contributes to the reverse of the bow out of dislocations between obstacles (Friedel, 1953; Mott, 1952). More distinguishable from the elastic strain scale is the influence of partly reversible dislocation mechanisms like Orowan looping or prismatic loops from interactions with particles, and reversing dislocation sources when the load is reversed (Van Dokkum et al., 2021). In theory, the emitted loops from a Frank-Read source would, without other interactions, shrink back to the source and a similar number of opposite loops will be generated. The stress contribution from dislocations that pile up towards grain boundaries or other obstacles vanishes when the load is reversed,

and the build-up of opposite pileups requires a certain small straining in the reverse loading mode before contributing to the yield stress. In high-resolution crystal plasticity simulations, this phenomenon can in principle be captured based on strain gradient plasticity (Erdle and Boehlke, 2023; Wulfinghoff et al., 2015). Without the added complexity of the gradient plasticity, such mechanisms justify models with kinematic hardening of the slip systems, where the critical resolved shear stress gains extra strength during loading as compared to that of its reverse slip system, as suggested by Peeters et al. (2001) for polarization of cell wall dislocation structures in IF-steels, and in more phenomenological models (Holmedal et al., 2008; Kitayama et al., 2013; Rauch et al., 2007; Sharma et al., 2022; Zecevic and Knezevic, 2015). Both the kinematic hardening of the slip systems and the composite of elastically and plastically loaded grains provide qualitative mechanisms and explanations for the anelastic behavior. A key question is whether both are equally important.

Amongst the more recent investigations, the group of Khan (Iftikhar et al., 2021; Khan et al., 2009, 2010a, 2010b) has conducted experimental studies on the evolution of the subsequent yield surfaces and elastic constants on low (AA6061-T6511) and high (AA1100) work-hardening alloys and on an annealed AA6061 alloy. They used a $10\mu\varepsilon$ strain offset definition to identify yielding after unloading and reloading for several levels of pre-deformations.

Along with the experimental studies of the yield surfaces at small plastic strains, crystal plasticity models have been employed to study the subsequent yielding of polycrystalline materials. These models can be distinguished into two groups. Works without a backstress term for the critical resolved shear stress have so far been analysed by Taylor type aggregate models, either as stand-alone for single strain paths (Hutchinson, 1970; Iftikhar et al., 2021; Lin and Ito, 1965; Radi and Abdul-Latif, 2012; Schurig et al., 2007) or coupled with finite element formulations (Iftikhar et al., 2021, 2022). Considering a backstress term for the critical resolved shear stress, Hu et al. (2015) calculated yield-surface sections by simulating shear and normal stresses of a quasi-three-dimensional ring section using rate-independent CPFEM. In a recent investigation, Lu et al. (2020) made a coarse-meshed CPFEM model of a torsion-tension test of an entire thin-walled tube using 36000 elements representing one grain each for a random texture. They found that the results were similar to when using a representative volume element (RVE) with 125 grains meshed by 27000 elements, applying periodic boundary conditions. A backstress for each slip system was required for calibration of the considered commercial pure polycrystalline aluminium alloy.

The present study uses the full-field, crystal-plasticity software DAMASK (Roters et al., 2019) to calculate yield-surface sections at small probing strains. The DAMASK spectral solver allows a high spatial resolution with shorter computational time compared to CPFEM but requires periodic boundary conditions. Hence, the yield-surface sections need to be calculated based on crystal-plasticity simulations of an RVE. In addition, a simpler rate-dependent Taylor-Lin type aggregate model (Lin, 1957) is used to see how the results compare to the simulations by a mean-field solver. The contribution to the Bauschinger effect by including a model for the backstress of the slip systems is investigated and discussed. As mentioned above, models for latent softening of reverse slip systems are known from the literature. Here one such model (part of the DAMASK implementation) is applied at very small strains to model the elastoplastic transition. Simple prestrains in proportional load and a prestrain by a series of two subsequent strain paths are considered. The influence on the corresponding yield surface of the material strength, the work hardening, and the initial texture is analysed.

2. Virtual experiments

The spectral full-field solver of the DAMASK software (Roters et al., 2019) is used to model the constitutive behaviour of polycrystals. A representative volume containing 376 grains is synthesized for calculating selected yield-surface sections. Models are tested with and without the Bauschinger effect on the slip system level. For comparison, selected cases are also calculated by a rate-dependent Taylor-Lin aggregate model. The latter model applies the same constitutive equations as in DAMASK but is formulated as a co-rotational hypo-elastic crystal-plasticity model. Hence, the stiffness tensor relates the Cauchy stress rate and the elastic part of the velocity gradient tensor, whereas, in DAMASK, it relates the second Piola-Kirchhoff stress tensor and the Green-strain tensor in the intermediate configuration. Since elastic strains are small in metals, the difference is negligible; therefore, the same stiffness tensor is applied for both models in the current work.

2.1. Crystal plasticity constitutive model

A brief description of the governing equations is provided, while it is referred to Roters et al. (2019) for more detailed information. The total deformation gradient can be decomposed into elastic and plastic parts multiplicatively as

$$\boldsymbol{F} = \boldsymbol{F}_e \cdot \boldsymbol{F}_p \tag{1}$$

where $\boldsymbol{F}_e$ represents rigid body rotation and elastic distortion of the crystal lattice and $\boldsymbol{F}_p$ covers the plastic shear deformations due to slip on specific crystalline planes in corresponding Burgers vector directions. The second Piola-Kirchhoff stress, $\boldsymbol{S}$, in the intermediate configuration is related linearly to the Green strain, $\boldsymbol{E}_e = \left(\boldsymbol{F}_e^T \cdot \boldsymbol{F}_e - \boldsymbol{I}\right)/2$ as

$$\boldsymbol{S} = \mathbb{C} : \boldsymbol{E}_e \tag{2}$$

where $\mathbb{C}$ is the fourth-order elastic stiffness tensor and $\boldsymbol{I}$ is the second-order identity tensor. The plastic velocity gradient $\boldsymbol{L}_p$ is given by the slip activity as

$$\boldsymbol{L}_p = \dot{\boldsymbol{F}}_p \cdot \boldsymbol{F}_p^{-1} = \sum_{\alpha=1}^{N} \dot{\gamma}^\alpha \boldsymbol{b}^\alpha \otimes \boldsymbol{n}^\alpha \tag{3}$$

where N is the number of slip systems, counting both negative and positive slip directions. $\dot{\gamma}^\alpha$ displays the shear rate on slip system α indicated by the two-unit vectors $\boldsymbol{n}^\alpha$ (slip plane normal) and $\boldsymbol{b}^\alpha$ (slip direction). The rate-dependent plastic flow evolution on a slip system is modelled similarly to Wollmershauser et al. (2012) but here in a rate-dependent formulation that is implemented in the DAMASK software.

$$\dot{\gamma}^\alpha = \dot{\gamma}_0 \left\langle \frac{\tau^\alpha - g_{\mathrm{bs}}^\alpha}{g_{\mathrm{for}}} \right\rangle^{1/m} \tag{4}$$

here $\langle x \rangle = \max(x, 0)$ denotes the Macauley brackets, and $\tau^\alpha = \boldsymbol{S} : (\boldsymbol{b}^\alpha \otimes \boldsymbol{n}^\alpha)$ is the resolved shear stress, where α is numbering the 24 fcc slip systems $\{111\}\langle\bar{1}10\rangle$, counting both backward and forward slip directions. Furthermore, g_{bs}^α is the backstress, $\dot{\gamma}_0$ denotes a reference shear-strain rate and m is the strain-rate sensitivity. The 'forest' slip resistance g_{for} and the backstress g_{bs}^α evolve asymptotically towards $g_{1,\mathrm{for}}$ and $g_{1,\mathrm{bs}}$, respectively. The following relationships can formulate a behaviour similar to the one described by Wollmershauser et al. (2012):

$$g_{\mathrm{for}} = g_{1,\mathrm{for}} \left(1 - \exp\left(- \frac{\theta_{0,\mathrm{for}} \Gamma}{g_{1,\mathrm{for}}} \right) \right) + g_{0,\mathrm{for}} \tag{5}$$

$$\dot{g}_{\mathrm{bs}}^\alpha = \theta_{0,\mathrm{bs}} \exp\left(- \frac{\gamma^\alpha \theta_{0,\mathrm{bs}}}{g_{1,\mathrm{bs}}} \right) (\dot{\gamma}^\alpha - \dot{\gamma}^{\alpha'}), \qquad g_{\mathrm{bs}}^\alpha(t=0) = 0 \tag{6}$$

Slip system α' is the reverse slip system of α. $\theta_{0,\mathrm{for}}$ and $\theta_{0,\mathrm{bs}}$ denote the reference self-hardening coefficients and $\Gamma = \sum_\alpha \gamma^\alpha$ and $\gamma^\alpha = \int \dot{\gamma}^\alpha dt$. The initial 'forest' slip resistance is $g_{0,\mathrm{for}}$. Cases without backstress are covered by the same formulation by setting $\theta_{0,\mathrm{bs}} = 0$ (and any non-zero

$g_{1.bs}$). The Taylor model implementation only has this simplified version implemented.

2.2. Material hardening parameters and model set-up

Four cases without backstress are studied: weak without hardening, weak with hardening, strong without hardening, and strong with hardening. Their corresponding hardening parameters are listed in Table 1. Furthermore, one case with backstress is included with hardening parameters listed in Table 2. To investigate the effect of texture, four distinct axi-symmetric textures and a random texture were employed. The selected axisymmetric fibre textures, <100>, <111> and <100> + <111>, are typical for thin-walled tubes that are used for torsion-tension-compression tests to probe yield-surface sections. Their inverse pole figures are shown in Fig. 1. The DREAM3D microstructural software analysis package (Groeber and Jackson, 2014) was used to generate the RVE with 376 grains (Fig. 2). Due to the local formulation of the classical crystal plasticity theory, the size of the RVE is arbitrary, i.e., the same result will be obtained by increasing the side length of the RVE by any factor and keeping the same average strain rate. The equivalent sphere diameter of the grains in the RVE in Fig. 2, setting the volume equal to 1 mm^3, obeys an approximately normal distribution that then would have a mean diameter equal to 168.7μm and a standard deviation of 24.7μm. Periodic boundary conditions were applied.

2.3. Yield-surface section calculations

The virtual test sequence consists of first a prestrain imposed by a prescribed stress path to the desired strain level. At the end of the prestrain, the total strain is kept constant, allowing a stress relaxation for 1 h. After that, a reverse stress path with unloading through the elastic region is performed until reaching a point on the opposite side of the yield surface with 10$\mu\varepsilon$ plastic strain offset from the elastic curve. Next, the sequence simulation is rerun, but the unloading step is stopped in the middle between the relaxed stress point and the reverse yielding point. This point is inside the elastic region and is taken as the centre, from which various loading directions can then be probed. During an experimental determination of the yield surface, all points on the yield surface would be probed in a series, returning to the elastic region between each new yield point obtained in various stress directions. This methodology results in some accumulation of small plastic strains during the probing of the yield points, and only a few points can be measured. In the simulations, this source of error is avoided by repeating an independent sequence for each point, i.e., for each probed loading direction, the sequence of loading steps towards the yield surface centre during the pre-deformation. For all calculated yield-surface sections, 360 evenly distributed strain paths were probed this way.

To characterize the yield behaviour, the linear elastic trend and the deviation from elasticity are calculated similarly as in experiments. They are approximately equal to a deviation from a linear relation between the Von Mises effective stress and strain relation. The DAMASK code uses the first Piola-Kirchhoff stress, $\boldsymbol{P}$, in the prescribed mixed boundary condition. Hence, piecewise proportional strain paths in the $\sigma_{11} - \sigma_{12}$ section of the yield surface is considered by imposing the following

Table 1
Material properties used in the crystal plasticity modelling for cases without back stress ($\theta_{0.bs} = 0$, and an arbitrary $g_{1.bs}$). For all cases, the non-zero elasticity parameters are $C_{11} = 104.55$ GPa, $C_{12} = 52.25$ GPa and $C_{44} = 26.15$ GPa, the strain rate sensitivity is $m = 0.01$ and $\dot{\gamma}_0 = 0.01\ s^{-1}$.

Case	$\theta_{0.for}$ (MPa)	$g_{0.for}$ (MPa)	$g_{1.for}$ (MPa)
Weak, without hardening	0	10	–
Weak, with hardening	440	10	12
Strong, without hardening	0	100	–
Strong, with hardening	440	100	120

Table 2
Material properties used in the crystal plasticity modelling of the case by Iftikhar et al. (2021). For all cases, the elasticity parameters are $C_{11} = 104.55$ GPa, $C_{12} = 52.25$ GPa and $C_{44} = 26.15$ GPa, the strain rate sensitivity is $m = 0.01$ and $\dot{\gamma}_0 = 0.001\ s^{-1}$.

Case	$\theta_{0.for}$ (MPa)	$g_{0.for}$ (MPa)	$g_{1.for}$ (MPa)	$\theta_{0.bs}$ (GPa)	$g_{1.bs}$ (MPa)
Without backstress	500	26	96.5	0	–
With backstress	550	9	16	250	18

mixed boundary condition for the probing load from the yield-surface section centre:

$$\dot{\overline{\boldsymbol{F}}} = \begin{bmatrix} \dot{e} & \dot{\gamma} & * \\ 0 & * & * \\ 0 & 0 & * \end{bmatrix}, \qquad \overline{\boldsymbol{P}} = \begin{bmatrix} * & * & 0 \\ * & 0 & 0 \\ * & * & 0 \end{bmatrix} \tag{7}$$

here the "$*$" means unknown, $\dot{e}$ is the nominal normal strain rate and $\dot{\gamma}$ is the engineering shear strain rate. The deformation gradient tensor at the start of the probing, i.e., at the yield-surface centre, equals $\boldsymbol{F}_c$. To measure the probing strain, a new deformation gradient $\widetilde{\boldsymbol{F}}$ is introduced, which is re-initialized to the identity tensor at the time when reaching the yield-surface centre, i.e., it obeys $\dot{\widetilde{\boldsymbol{F}}} = \boldsymbol{L}\cdot\widetilde{\boldsymbol{F}}$, which is the same equation as $\boldsymbol{F}$, but with another initial condition (i.e., $\widetilde{\boldsymbol{F}} = \boldsymbol{F}\cdot\boldsymbol{F}_c^{-1}$). Using the condition (Eq. (7)), all Cauchy stress components, except σ_{11} and σ_{12} remain approximately equal to zero during the small probing stresses considered. An equivalent von Mises stress can be calculated from σ_{11} and σ_{12} as $\sigma_{vM} = \sqrt{\sigma_{11}^2 + 3\sigma_{12}^2}$, and the von Mises strain is estimated as

$$\varepsilon_{vM} = \frac{1}{\sqrt{3}}\sqrt{\left((\widetilde{F}_{11}-1)^2 + (\widetilde{F}_{22}-1)^2 + (\widetilde{F}_{33}-1)^2\right) + \widetilde{F}_{12}^2}. \tag{8}$$

Due to the elasticity relation, assuming a linear relation between the 2nd Piola-Kirchhoff stress and the Green strain, a quadratic fitting is made to capture the elastic part of the von Mises stress-strain curve, from which an offset of 10$\mu\varepsilon$ is taken as the yield point.

Since the quadratic term is unsuitable for describing the elastic trend beyond relatively small extrapolations, a linear curve is applied when considering larger offsets. This does not cause much error since when the offset is larger, the deviation from linearity between the Cauchy stress and the von Mises strain becomes very small compared to the offset itself.

3. Results

The models were used to calculate the σ_{11} - $\sqrt{3}\sigma_{12}$ section of the yield surface, a section that combinations of torsion, tension, and compression of thin-walled tubes can measure. Examples of typical texture components for axisymmetric tubes are calculated. Materials with different combinations of with or without work hardening and high or low strength are also included in the investigation. The pointed vertex appears only after a pre-deformation, but only a small plastic strain is required to establish the vertex. The influence of pre-deformations in different directions, different amounts of prestrain, and a pre-deformation with an abrupt strain-path change during the prestrain are investigated by relevant example cases. Some cases are calculated both with the DAMASK full-field approach and compared to the Taylor-Lin mean field model solutions.

3.1. Influence of strength and work hardening

Yield-surface sections for a Von Mises prestrain of 2%, in tensile (Fig. 3a) or shear (Fig. 3b) mode, are plotted. The four cases without a backstress in Table 1 are compared for the case of a random texture. It is

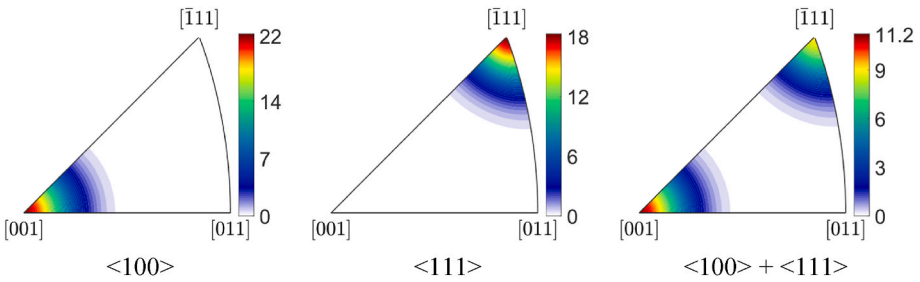

Fig. 1. Inverse pole figures showing the tensile axis for the three different axisymmetric fibre textures.

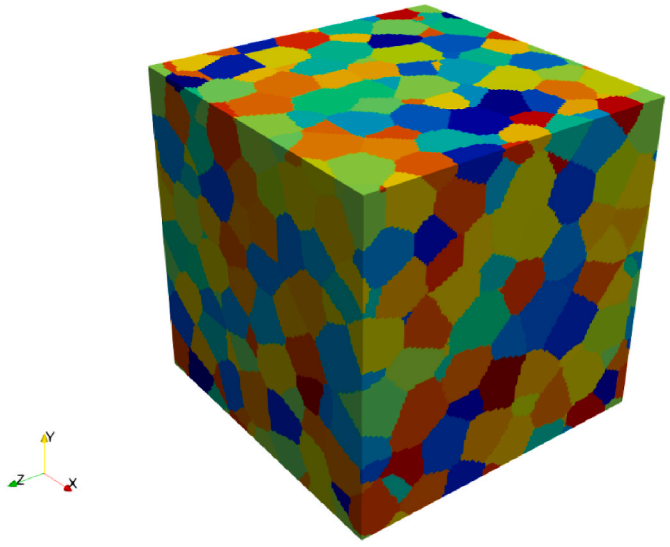

Fig. 2. The RVE consisting of 376 randomly oriented grains with a spatial resolution of 128 × 128 × 128. A colour scale for the first Euler angle is used to distinguish the grains. (For interpretation of the references to colour in this figure legend, the reader is referred to the Web version of this article.)

seen that regardless of the types of strength and work hardening, a moderate Bauschinger effect is observed, where the yield-surface sections enclose the origin for all the cases in Fig. 3. Due to the elastoplastic composite effect, strongly distorted and anisotropic yield-surface sections are seen with $10\mu\varepsilon$ strain deviation from elasticity. Interestingly, the pointed vertex in the loading direction is significantly rounded, for both preloading directions in Fig. 3. The yield surfaces are normalized by the stress at the tip of the rounded pointed vertex in the loading direction. The work hardening does not make much of a difference for the case with a prestress by shear. However, the stronger material has a smaller yield surface with a stronger Bauschinger effect.

3.2. Yield-surface sections at different prestrains and probing strains

Fig. 4 shows yield-surface sections for a random texture after a 2% von Mises prestrain. To obtain a stress direction for which $\sigma_{11} = \sqrt{3}\sigma_{12}$, a ratio $\dot{\gamma}/\dot{e} = 2.075$ was applied during the prestrain at a von Mises strainrate of 10^{-5}s^{-1}.

The yield-surface sections in Fig. 4 are all normalized by the σ_{11} yield stress of the outer yield surface (10000 $\mu\varepsilon$). Four different offsets from the elastic strain (10, 100, 1000, and 10000 $\mu\varepsilon$) are included. With a small offset, the distortions of the yield loci are stronger, while at higher offsets, the distortions vanish. The pointed vertex is rounded, but the tip almost touches the outer locus (10000 $\mu\varepsilon$) for all offsets.

The result of different pre-straining on the yield loci is plotted in Fig. 5 for the strong material without hardening (Table 1). It is interesting to note that when the yield surface is normalized by the σ_{11} stress

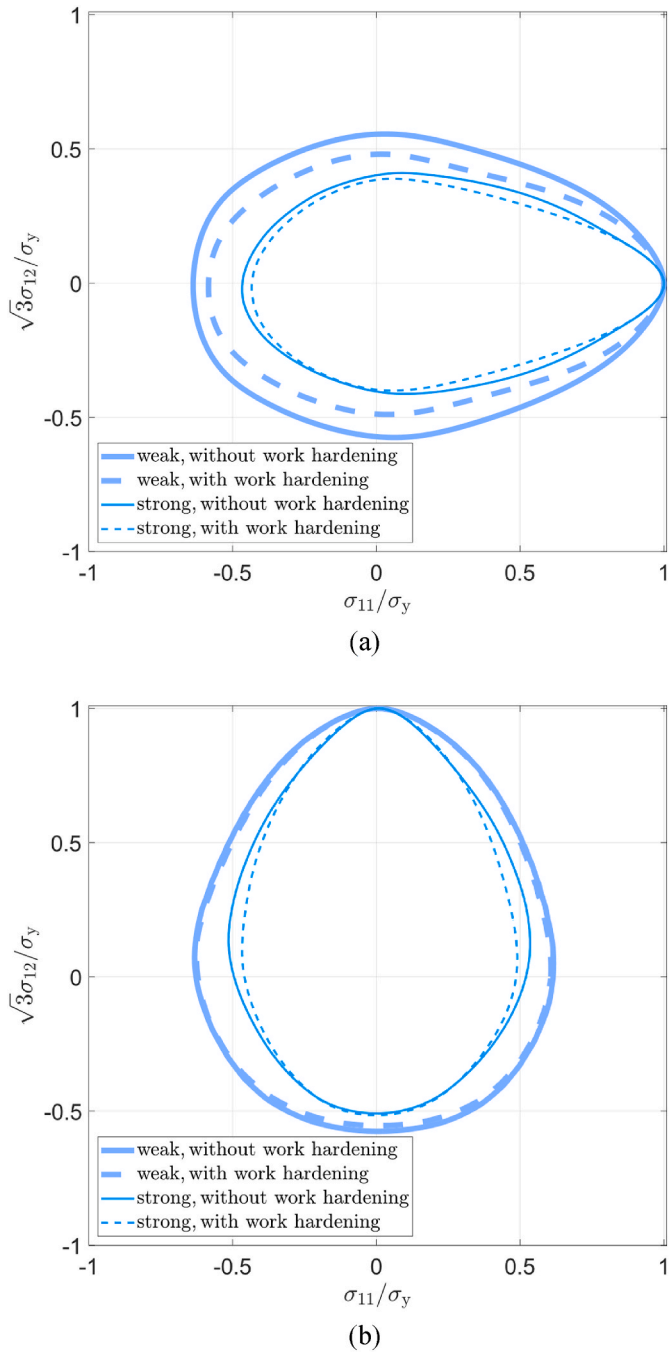

Fig. 3. Yield-surface sections for a random texture comparing the four cases without backstress in Table 1 (a): after 2% of engineering tensile prestrain in the tensile direction, (b): after 2% of engineering shear-prestrain.

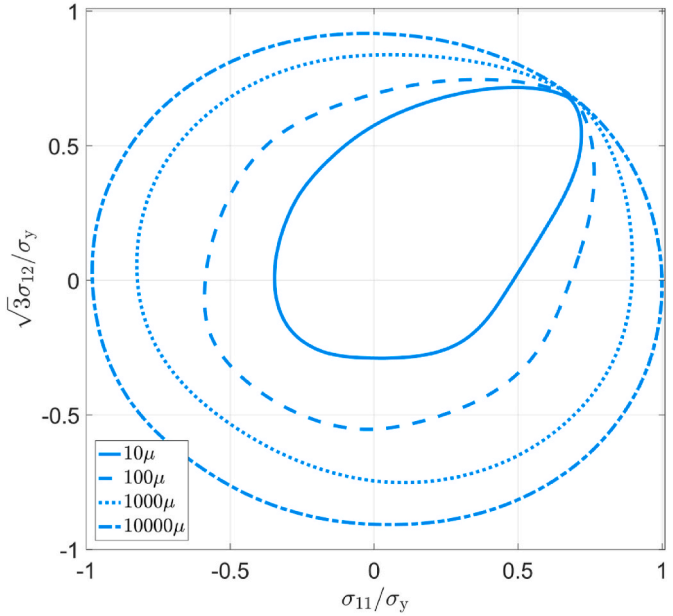

Fig. 4. Yield loci after applying a 2% of prestrain along $\sigma_{11} = \sqrt{3}\sigma_{12}$ stress direction for four different offsets from elasticity. For random texture and strong material without hardening.

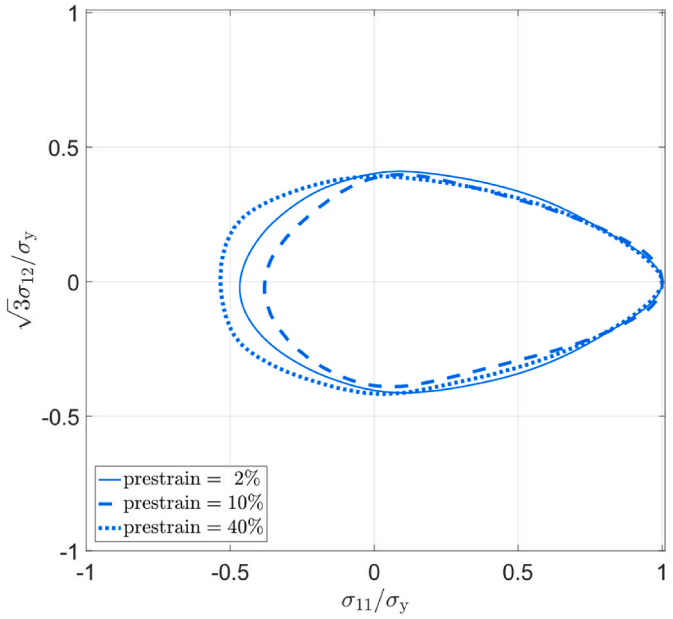

Fig. 5. Yield-surface sections for 2%, 10%, and 40% tensile prestrains. For the comparison, each yield surface is normalized by the σ_{11} stress for $10\mu\varepsilon$ offset from elastic linearity. A random texture and a case with strong material without hardening are considered here.

for $10\mu\varepsilon$ strain offset from elastic linearity at the tip of the rounded pointed vertex, there is no significant difference between the shape of the yield surface between 2%, 10%, and 40% tensile prestrain.

3.3. Influence of a strain-path change during the pre-deformation

In Fig. 6, yield-surface sections obtained after a two-step pre-deformation are plotted for the strong material without hardening. Firstly, a prestress in the shear direction is performed, then unloaded to an elastic point in the centre of the yield surface. The next part of the pre-deformation is in the tensile direction, which then is unloaded to an elastic point in the centre of the yield locus, from which the probing in 360 stress directions is made to plot the instant 10μ yield-surface section. Additionally, the $10\mu\varepsilon$ yield-surface section after the first pre-deformation step (shear direction) and the initial $10\mu\varepsilon$ and $2000\mu\varepsilon$ yield-surface section without any pre-deformation are also shown in the figure.

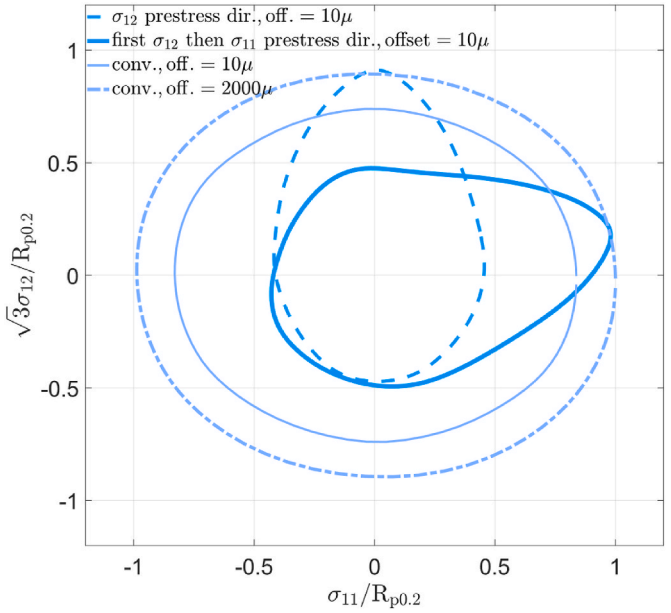

Fig. 6. Yield-surface sections for the "strong, with work hardening" case (Table 1) and a random texture with the offset strain from elasticity and the prestress directions indicated by the respective legends. The amounts of pre-strains were 2% shear strain (thick dashed line) and 4% for the two-step: 2% shear strain, then 2% tensile strain (thick solid line). The initial yield stress $(R_{p0.2})$ (i.e., with offset $= 2000\mu\varepsilon$) is chosen for the normalization.

3.4. Influence of the texture

The same yield-surface sections as in Fig. 3a, for the strong and weak cases without work hardening and with random texture, were calculated both by the spectral crystal-plasticity solver and by the statistical Taylor-Lin model implementation. The results are plotted in Fig. 7. Note that the stress of $10\mu\varepsilon$ offset from elastic linearity normalises the stress in the σ_{11} direction as calculated by the spectral solver (DAMASK). Without this normalization, the Taylor factor would be larger by the Taylor model than by the full-field spectral model (Zhang et al., 2019). However, when it comes to the shape of the yield surface, it can be noted that the full-field spectral method and the much simpler aggregate type of the Taylor model predict very similar subsequent yield-surface sections after 2% tensile prestrain.

To analyse the effect of texture on the evolution of yield surfaces after 2% tensile prestrain, the yield surfaces of four different textures are compared in Fig. 8. To produce the textures, the DREAM3D software was used. Three representative textures were synthesized as seen in Fig. 8. A <100> fibre with a maximum intensity of 22, a <111> fibre with a maximum intensity of 18, a combination of <100> and <111> fibre with maximum intensities of 11.2 and 9, respectively, were tested. A close agreement is found between the full-field (DAMASK) and the mean-field (Taylor-Lin) results for all considered textures (see Fig. 8).

The yield-surface section of the <100> fibre texture has little distortion, a wide body, and almost no Bauschinger effect. Also, the <111> texture has a weak Bauschinger effect but with a narrower rounded, pointed vertex. The random texture has the strongest Bauschinger effect and relatively the smallest and most distorted yield

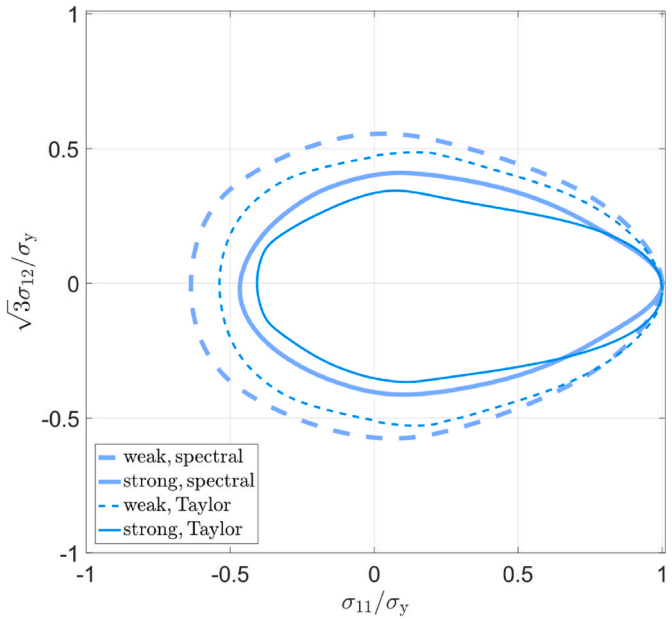

Fig. 7. A comparison of the spectral full-field and the Taylor-Lin aggregate model for calculations of the yield-surface section after 2% of tensile prestrain, for the cases of strong and weak materials without work hardening (see Table 1) for a random texture.

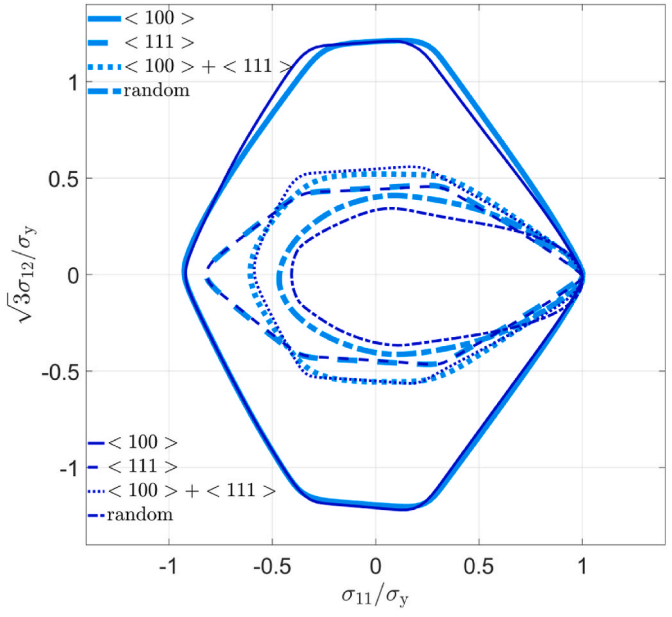

Fig. 8. Yield surfaces of four different textures, calculated by two distinct crystal-plasticity solvers: the spectral method (full-field, light blue lines) and the Taylor model (mean-field, dark blue lines). A tensile prestrain of 2% is applied. For the "strong without hardening" material. Each yield surface is normalized by the σ_{11} stress of $10\mu\varepsilon$ offset from elastic linearity. (For interpretation of the references to colour in this figure legend, the reader is referred to the Web version of this article.)

surface, while the mix of <100> and <111> is closer to the random than to <100> or <111>.

3.5. Influence of strain rate sensitivity

To investigate the influence of the strain rate sensitivity, m, three distinct yield surfaces for three strain rate sensitivities of $m = 10^{-2}$, 10^{-3}, and 10^{-6} are plotted in Fig. 9. It can be seen that there is a noticeable difference between yield surface with $m = 10^{-2}$ and the other two, where the smallest m gives a slightly sharper but still blunted pointed vertex. For m smaller than 10^{-2} the curve remains approximately unchanged.

3.6. Influence of including a backstress for each slip system and comparing with experiments

To investigate the role of the backstress of the slip systems, the hardening parameters were chosen so that the stress-strain curves for a tensile test were similar as for the AA6061 aluminium alloy, with a weak, nearly random texture, reported in Iftikhar et al. (2021). The backstress is calibrated to occur within a very small strain increment. Hence, it will affect the stress-strain curve only during the early elastoplastic transition. The stress-strain curves for the models with and without backstress were calibrated (Table 2) to match the measured one by Iftikhar et al. (2021). The stress-strain curve of the tensile test, and also a compression-tension curve with a prestrain of 2%, can be seen in Fig. 10a.

For the case of the tensile prestrain of 2%, the subsequent $10\mu\varepsilon$ yield surfaces for the cases with and without the backstress are compared with experimental and CPFEM results by Iftikhar et al. (2021) are plotted in Fig. 10b. In addition, the experimental results for a peak aged similar alloy by Khan et al. (2009) are included in Fig. 10b. The latter has a much stronger Bauschinger effect. The spectral solver of the DAMASK software is used for these simulations. For the case with a non-zero backstress, Fig. 10a reveals a more pronounced Bauschinger effect with a significantly longer-lasting transient in the reverse direction before reaching the similar level as in the forward direction. Similar to what can be observed experimentally, this will result in an anelastic hysteresis by unloading-reloading after some amount of stretching in a tensile test.

It can be seen from Fig. 10b that the backstress of the slip systems strengthens the Bauschinger effect significantly and gives results that are closer to the experiments than without the backstress. Note that this is in contradiction to the CPFEM results reported by Iftikhar et al. (2021), reporting a very strong Bauschinger effect without any reverse hardening in the model. Furthermore, the backstress of the slip systems

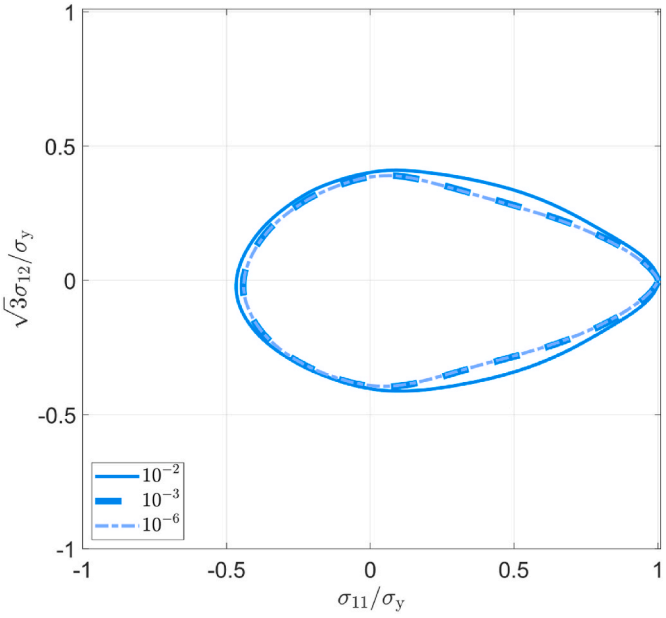

Fig. 9. Yield surface for three different strain rate sensitivities m for the strong material without work hardening.

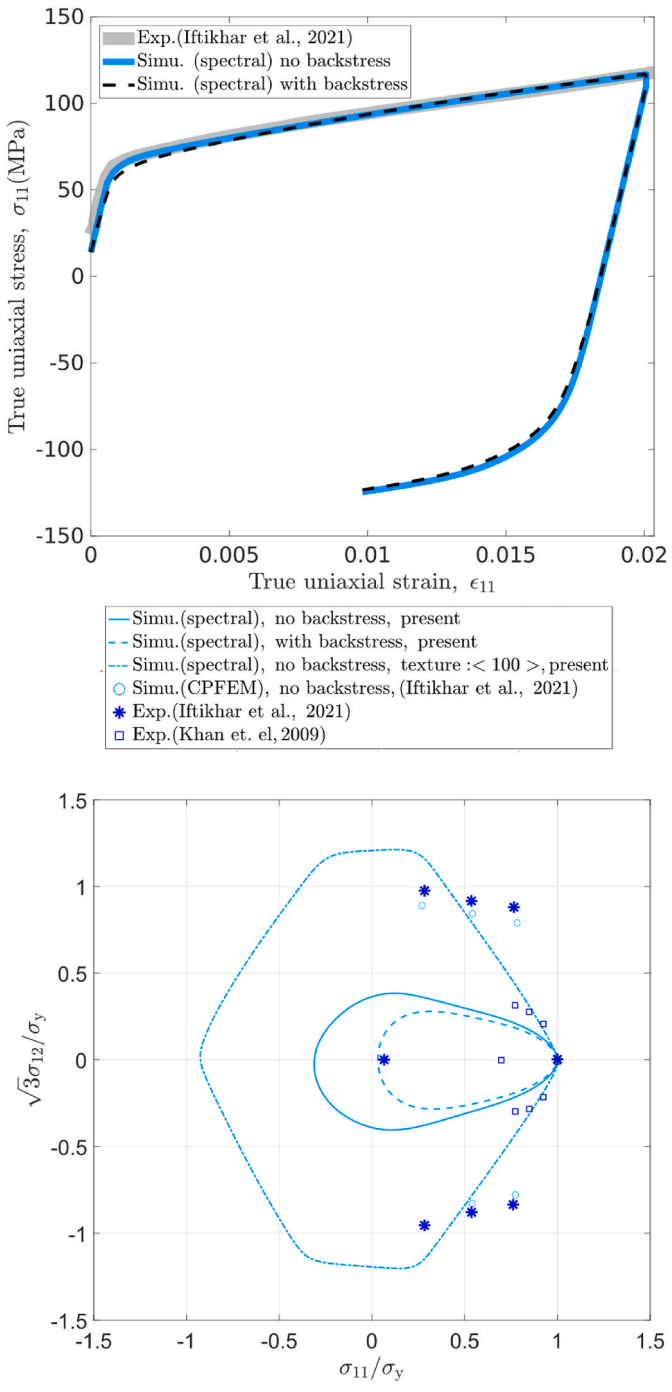

Fig. 10. (a): Comparison of experimental (Iftikhar et al., 2021) tension-compression curves and curves simulated by DAMASK for a random texture, using models with and without backstress of the critical resolved shear stress. Work hardening parameters for the simulated cases are found in Table 2 (b): Yield surface section, normalized by the tensile stress, σ_Y, for each considered yield surface with 10 $\mu\varepsilon$ offset after 2% tensile prestrain. Simulated cases are: random texture with and without backstress, <100> fibre texture without backstress. Experiments and CPFEM results for a weak texture by Iftikhar et al. (2021) and for a peak aged condition of a similar alloy by Khan et al. (2009).

results in a slightly narrower yield surface encompassed by the yield surface without the backstress.

4. Discussion

During a small increment of deformation, the 10$\mu\varepsilon$ yield surface develops a pointed vertex in the loading direction and a flattened shape in the reverse direction. This pointed vertex is directional, pointing approximately towards the current stress direction. The yield surface has a short-term memory of the most recent strain path but changes rapidly, where the vertex tries to catch up with the current loading path. Hence, the instant shape of the 10$\mu\varepsilon$ yield surface is found to be more complex during strain-path changes.

It is noted, that as compared to the rate-independent calculations of, e.g. Hutchinson (1970), the instant 10$\mu\varepsilon$ yield surface is more blunted with the strain ate sensitive viscoplastic calculations made here, even when applying a very small strain rate sensitivity of $m = 10^{-6}$. In experimental works, a certain time is required to glue the strain gages onto the specimen after the pre-deformation. During this period, 1 h in the present simulations, plastic relaxation occurs, which modifies the yield surface. The viscoplastic model applied in the DAMASK software does not account for any athermal contributions to the critical resolved shear stress. However, in more realistic physical-based models, one will expect an athermal, strain-rate independent part of the yield stress, e.g., from athermal strength contributions from particles. The athermal stress from the precipitates is obviously large for the case for the age hardened alloy investigated by Khan et al. (2009), for which the viscoplastic model would overestimate the plastic relaxation after the prestraining. This may contribute to an explanation why the measured 10$\mu\varepsilon$ yield surface by Khan et al. (2009) is relatively smaller than for the annealed conditions reported by Iftikhar et al. (2021) and smaller than the yield surfaces calculated in the current work.

Note that unless an evolution equation for the backstress of each slip system is part of the model, the yield surface of one single grain cannot reveal neither any Bauschinger effect nor a flattening of the reverse part of the yield surface. When a backstress of the slip systems is not included in the model, flattening and a pointed vertex can only occur in polycrystals, where the composite effect from a mix of elastically and plastically stressed grains is causing it. It follows that the shape of the yield surface of a material with a sharp texture will be less sensitive to the probing strain, whereas a yield surface with a random texture will change significantly with decreased probing strain. This is evident from the comparison in Fig. 10b of the calculations of the strong <100> fibre texture versus the random texture.

In this work, as opposed to the results reported by Iftikhar et al. (2021), only a limited Bauschinger effect in the 10$\mu\varepsilon$ yield surfaces is predicted without a backstress model. The simulations performed here (e.g., Fig. 3) show that neither the high strength nor the low work hardening of the age-hardening alloy can be responsible for the significant amount of Bauschinger effect that was measured by Iftikhar et al. (2021) and by Khan et al. (2009). However, these strong Bauschinger behaviours can be obtained by applying a backstress on the critical resolved shear stress. Note that this is a backstress that evolves and saturates during a very short strain increment and that the backstress therefore is fully developed before reaching the conventional yield limit ($R_{p0.2}$). It is reasonable to assume that a backstress of the critical resolved shear stress needs also to be considered and that this backstress might depend on the microstructure.

A backstress of each slip system can be required in models even for pure metals (Lopes et al., 2003; Peeters et al., 2001), for which microstructure characterization have revealed correlations between the Bauschinger effect and the building of a dislocation substructure during preloading. The dislocation structures are partly destroyed during the following strain reversal, before a similar type of structure is rebuilt during the new strain path. Note however, that for this type of

mechanisms, the strain scale required for the transient of the backstress subsequent to the strain path change lasts significantly longer than the elastoplastic transition. In the presence of particles, a strong Bauschinger effect may be found even in single crystals, see e.g. Gould et al. (1974). Hence, for a variety of mechanisms and strain scales, a model for the backstress of the critical resolved shear stress is important to correctly predict phenomena like spring back and anelasticity in alloys. The detailed physical mechanism for the backstress of the slip system will vary from alloy to alloy. Both dislocation structures, interaction with non-shearable particles and composite effects may contribute. All these mechanisms can be modelled by phenomenological models for the backstress of the slip systems, like with Eqns. (4-7).

With or without a backstress for the slip systems as part of the model, a single crystal or a very sharp texture will, due to the lack of a mix of elastic and plastic loaded grains, not develop a well-defined pointed vertex during the pre-deformation. For the case with the strong <100> fibre texture, the region of the yield surface close to the loading direction remains almost similar to the yield surface obtained with larger probing strains. This dependency on the texture sharpness is interesting in terms of formability, as it suggests that when a sheet with a strong texture is stretched in biaxial tension, it might require a larger perturbation, e.g., thickness variation, for instability to occur at a given strain. Of course, keeping in mind that the texture itself will strongly influence the mechanical anisotropy and hence the formability. The pointed vertex becomes blunter with a strong texture, while a sharper pointed vertex would provide a simpler way to change the strain path locally, after which the unstable plane-strain deformation mode could evolve. Hence the sharpness of the texture is important when modelling instability phenomena like the formation of shear bands, plastic buckling, or flow instabilities in the biaxial region of the formability diagram. In these cases, the crystal plasticity models will provide results that the current continuum-plasticity flow theory cannot capture.

Latent hardening of other slip systems than the reverse ones might also influence the 10μ offset yield surface. New slip systems must be activated when changing the strain path into strain directions that are nearly orthogonal to the first strain path. As suggested by Holmedal et al. (2008), the systematic latent hardening of passive slip systems will expand the crystal yield surface in regions orthogonal to the loading direction. This will also make the pointed vertex more rounded, independently of the texture. This topic goes beyond the scope of the current investigation but is interesting for future studies. The only latent hardening considered in this work, except the isotropic kind from all the slip systems, is the kinematic hardening of slip systems, i.e., a softening of the reverse slip systems.

As Li and Wagoner (2021) pointed out, the anelasticity, which plays an important role in spring-back predictions, can be explained by the kinematic hardening of the slip systems. The calculations here suggest that this mechanism is also required to explain the strong flattening of the part of the yield surface in the reverse of the preloading stress direction when the yield surface is probed at small offset strains. This may involve a back stress that develops and saturates during the elastoplastic transition. Experimentally, e.g. (Hecker, 1976; Iftikhar et al., 2021; Khan et al., 2009, 2010a, 2010b; Kuroda, 2022; Kuwabara et al., 2000; Naghdi and Rowley, 1954; Phillips and Lee, 1979; Phillips and Moon, 1977; Phillips and Ricciuti, 1976), this effect is reported to be very strong, where the measured yield-surface sections in most cases do not even include the origin. Iftikhar et al. (2021) reported a strong Bauschinger effect by their crystal-plasticity calculations without kinematic hardening of the slip systems. However, the simulation results reported in other investigations (Hutchinson, 1970; Lin and Ito, 1965; Radi and Abdul-Latif, 2012; Schurig et al., 2007) are consistent with what is reported here, i.e., that without (rapid) kinematic hardening of the slip systems, the estimated Bauschinger effect is significantly smaller than what is measured.

Khan and co-workers investigated the effect of work hardening on the yield surfaces at small probing strains (Khan et al., 2009, 2010a, 2010b). However, the annealed commercial pure alloy with strong work hardening is much weaker than the compared age-hardened AlMgSi alloy. The simulation results reported here suggest that the difference in strength rather than the difference in work hardening makes the shape of the yield-surface sections different. With increased strength, the 10μ yield surface becomes relatively narrower (Fig. 3). The reason for this difference is that the elastic strain range is increased, and the balance between contributions from elastically and plastically loaded grains is altered. As discussed above, the difference between these alloys in terms of the Bauschinger effect cannot be captured without kinematic hardening of the slip systems.

Interestingly, the shape of the $10\mu\varepsilon$ yield-surface sections calculated with the viscoplastic Taylor-Lin mean-field model is very similar to the sections calculated by the full-field crystal plasticity model (DAMASK), indicating that the Taylor homogenization is applicable at small plastic strains in the elastoplastic transition. Note, however, that the Taylor factors are different (Mánik et al., 2015), hence the size of the yield surfaces are different. Still, including a backstress for each slip system seems more important for the results than running the far more expensive full-field simulations. The current approach is too computational demanding for a direct application in forming simulations. As compared to a continuum plasticity model, also the Taylor-Lin model is computationally demanding, but it can in some cases be directly applied to forming simulations, e.g., in Marcinak-Kuczynski analysis of biaxial flow instabilities or as part of a finite element code.

5. Conclusions

Yield surfaces have been calculated by a full-field crystal plasticity model, using a probing strain of $10\mu\varepsilon$ von Mises offset strain. The differences between using a mean-field viscoplastic Taylor-Lin model and a full-field spectral solver in predicting the shape of these yield surfaces at small probing strains within the elastoplastic transition are relatively small. They both reveal a flattening of the reverse part and a pointed vertex in the loading direction. The pointed vertex is, however, significantly rounded (after stress relaxation). It is found that the blunt tip of the pointed vertex does not vanish with decreasing strain rate sensitivities. The work hardening does not affect the shape of these yield surfaces significantly, while a stronger material shows a relatively smaller yield surface (normalized by the tip of the rounded, pointed vertex) and a slightly stronger Bauschinger effect.

The main conclusion from this work is that a kinematic hardening of the critical resolved shear stress, occurring during a very short strain scale, is required to qualitatively reproduce the strong Bauschinger effect as earlier reported for measured yield-surface sections. It can be concluded that for a realistic description of spring back and anelasticity caused by the elastoplastic transition, the kinematic hardening of the slip systems is important to include in crystal plasticity simulations.

Another significant conclusion is that the sharpness of the texture plays an important role, where a more random texture gives a sharper pointed vertex. This makes a weakly-textured alloy more prone to flow instabilities like biaxial necking, shear-band formation, and plastic buckling. The crystal-plasticity simulations provide a description of the elastoplastic transition and the instant yield surface that are important for accurately describing flow instabilities, spring-back, and anelasticity. The current continuum-plasticity flow theory needs to be further developed to capture this.

CRediT authorship contribution statement

Arash Imani Aria: Writing – review & editing, Writing – original draft, Visualization, Validation, Software, Methodology, Conceptualization. **Bjørn Holmedal:** Writing – review & editing, Supervision, Methodology, Conceptualization. **Tomáš Mánik:** Writing – review & editing, Supervision, Methodology, Conceptualization. **Knut Marthinsen:** Writing – review & editing, Supervision, Project

administration, Methodology, Conceptualization.

Declaration of competing interest

The authors declare that they have no known competing financial interests or personal relationships that could have appeared to influence the work reported in this paper.

Data availability

No data was used for the research described in the article.

Acknowledgments

In this research, the computations were performed on resources provided by the NTNU IDUN/EPIC computing cluster (Själander et al., 2019). A.I.A. acknowledges funding from the NTNU Digitalization Transformation initiative through the project 'AllDesign.' T.M. acknowledges funding from the METPLAST project, supported by the Research Council of Norway, FRIPRO grant 315727. K.M. acknowledges funding from the Research Council of Norway through the Center for Research based Innovation SFI PhysMet (grant 309584). We also thank Jan Christian Meyer from the Department of Computer Science, NTNU, for assistance with preparing DAMASK software for the supercomputers.

References

Aria, A.I., Mánik, T., Holmedal, B., Marthinsen, K., 2023. A computational study on efficient yield surface calibrations using a crystal plasticity spectral solver. Multiscale Multi Mod.
Barlat, F., Gracio, J.J., Lee, M.G., Rauch, E.F., Vincze, G., 2011. An alternative to kinematic hardening in classical plasticity. Int. J. Plast. 27, 1309–1327.
Barlat, F., Yoon, S.-Y., Lee, S.-Y., Wi, M.-S., Kim, J.-H., 2020. Distortional plasticity framework with application to advanced high strength steel. Int. J. Solid Struct. 202, 947–962.
Batdorf, S.B., 1949. Theories of plastic buckling. J. Aeronaut. Sci. 16, 405–408.
Bishop, J.F.W., Hill, R., 1951. A theoretical derivation of the plastic properties of a polycrystalline face-centred metal. Philos. Mag. A 42, 1298–1307.
Bong, H.J., Lim, H., Lee, M.G., Fullwood, D.T., Homer, E.R., Wagoner, R.H., 2017. An RVE procedure for micromechanical prediction of mechanical behavior of dual-phase steel. Mat Sci Eng a-Struct 695, 101–111.
Chaboche, J.L., 2008. A review of some plasticity and viscoplasticity constitutive theories. Int. J. Plast. 24, 1642–1693.
Christoffersen, J., Hutchinson, J.W., 1979. A class of phenomenological corner theories of plasticity. J. Mech. Phys. Solid. 27, 465–487.
Erdle, H., Boehlke, T., 2023. Analytical investigation of a grain boundary model that accounts for slip system coupling in gradient crystal plasticity frameworks. P Roy Soc a-Math Phy 479.
Friedel, J., 1953. Anomaly in the rigidity modulus of copper alloys for small concentrations. Philos. Mag. A 44, 444–448.
Gotoh, M., 1985. A simple plastic constitutive equation with vertex effect. Eng. Fract. Mech. 21, 673–684.
Gould, D., Hirsch, P.B., Humphreys, F.J., 1974. Bauschinger effect, work-hardening and recovery in dispersion-hardened copper crystals. Philos. Mag. A 30, 1351–1377.
Groeber, M.A., Jackson, M.A., 2014. Dream. 3D: a digital representation environment for the analysis of microstructure in 3D. Integrating materials and manufacturing innovation 3, 56–72.
Han, F.B., Diehl, M., Roters, F., Raabe, D., 2020. Using spectral-based representative volume element crystal plasticity simulations to predict yield surface evolution during large scale forming simulations. J. Mater. Process. Technol. 277.
Hecker, S.S., 1976. Experimental studies of yield phenomena in biaxially loaded metals [Review]. In: Conference: Annual Meeting of the American Society of Mechanical Engineers, New York, NY, USA, 29 Nov 1976, United States, p. 33.
Hencky, H., 1924. Zur Theorie plastischer Deformationen und der hierdurch im Material hervorgerufenen Nachspannungen. ZAMM - Zeitschrift für Angewandte Mathematik und Mechanik 4, 323–334.
Hill, R., 1950. The Mathematical Theory of Plasticity. Clarendon Press, Oxford.
Hill, R., 1965. Continuum micro-mechanics of elastoplastic polycrystals. J. Mech. Phys. Solid. 13, 89–101.
Hill, R., 1967. Essential structure of constitutive laws for metal composites and polycrystals. J. Mech. Phys. Solid. 15, 79–95.
Holmedal, B., 2019. Bauschinger effect modelled by yield surface distortions. Int. J. Plast. 123, 86–100.
Holmedal, B., Van Houtte, P., An, Y.G., 2008. A crystal plasticity model for strain-path changes in metals. Int. J. Plast. 24, 1360–1379.
Hu, G., Huang, S., Lu, D., Zhong, X., Li, Z., Brocks, W., Zhang, K., 2015. Subsequent yielding of polycrystalline aluminum after cyclic tension–compression analyzed by experiments and simulations. Int. J. Solid Struct. 56, 142–153.
Hutchinson, J., 1970. Elastic-plastic behaviour of polycrystalline metals and composites. Proceedings of the Royal Society of London. A. Mathematical and Physical Sciences 319, 247–272.
Iftikhar, C.M.A., Khan, A.S., 2021. The evolution of yield loci with finite plastic deformation along proportional and non-proportional loading paths in an annealed extruded AZ31 magnesium alloy. Int. J. Plast. 143, 103007.
Iftikhar, C.M.A., Li, Y.L., Kohar, C.P., Inal, K., Khan, A.S., 2021. Evolution of subsequent yield surfaces with plastic deformation along proportional and non-proportional loading paths on annealed AA6061 alloy: experiments and crystal plasticity finite element modeling. Int. J. Plast. 143, 102956.
Iftikhar, C.M.A., Brahme, A., Inal, K., Khan, A.S.S., 2022. An evolution of subsequent yield loci under proportional and non-proportional loading path of 'as-received' extruded AZ31 magnesium alloy: experiments and CPFEM modeling. Int. J. Plast. 151.
Kassner, M.E., Geantil, P., Levine, L.E., 2013. Long range internal stresses in single-phase crystalline materials. Int. J. Plast. 45, 44–60.
Khan, A.S., Kazmi, R., Pandey, A., Stoughton, T., 2009. Evolution of subsequent yield surfaces and elastic constants with finite plastic deformation. Part-I: a very low work hardening aluminum alloy (Al6061-T6511). Int. J. Plast. 25, 1611–1625.
Khan, A.S., Pandey, A., Stoughton, T., 2010a. Evolution of subsequent yield surfaces and elastic constants with finite plastic deformation. Part II: a very high work hardening aluminum alloy (annealed 1100 Al). Int. J. Plast. 26, 1421–1431.
Khan, A.S., Pandey, A., Stoughton, T., 2010b. Evolution of subsequent yield surfaces and elastic constants with finite plastic deformation. Part III: yield surface in tension–tension stress space (Al 6061–T 6511 and annealed 1100 Al). Int. J. Plast. 26, 1432–1441.
Kitayama, K., Tome, C.N., Rauch, E.F., Gracio, J.J., Barlat, F., 2013. A crystallographic dislocation model for describing hardening of polycrystals during strain path changes. Application to low carbon steels. Int. J. Plast. 46, 54–69.
Koiter, W.T., 1953. Stress-strain relations, uniqueness and variational theorems for elastic-plastic materials with a singular yield surface. Q. Appl. Math. 11, 350–354.
Kuroda, M., 2022. Plastic flow localization resulting from yield surface vertices: crystal plasticity and corner theories of plasticity. Int. J. Material Form. 15, 43.
Kuroda, M., Tvergaard, V., 1999. Use of abrupt strain path change for determining subsequent yield surface: illustrations of basic idea. Acta Mater. 47, 3879–3890.
Kuroda, M., Tvergaard, V., 2001a. A phenomenological plasticity model with non-normality effects representing observations in crystal plasticity. J. Mech. Phys. Solid. 49, 1239–1263.
Kuroda, M., Tvergaard, V., 2001b. Shear band development predicted by a non-normality theory of plasticity and comparison to crystal plasticity predictions. Int. J. Solid Struct. 38, 8945–8960.
Kuwabara, T., Kuroda, M., Tvergaard, V., Nomura, K., 2000. Use of abrupt strain path change for determining subsequent yield surface: experimental study with metal sheets. Acta Mater. 48, 2071–2079.
Li, D.Y., Wagoner, R.H., 2021. The nature of yielding and anelasticity in metals. Acta Mater. 206, 116625.
Lin, T., Ito, M., 1965. Theoretical plastic distortion of a polycrystalline aggregate under combined and reversed stresses. J. Mech. Phys. Solid. 13, 103–115.
Lin, T.H., 1957. Analysis of elastic and plastic strains of a face-centred cubic crystal. J. Mech. Phys. Solid. 5, 143–149.
Liu, W.C., Pang, Y., 2021. A multi-scale modelling framework for anisotropy prediction in aluminium alloy sheet and its application in the optimisation of the deep-drawing process. Int. J. Adv. Manuf. Technol. 114, 3401–3417.
Lopes, A.B., Barlat, F., Gracio, J.J., Duarte, J.F.F., Rauch, E.F., 2003. Effect of texture and microstructure on strain hardening anisotropy for aluminum deformed in uniaxial tension and simple shear. Int. J. Plast. 19, 1–22.
Lu, D., Zhang, K., Hu, G., Lan, Y., Chang, Y., 2020. Investigation of yield surfaces evolution for polycrystalline aluminum after pre-cyclic loading by experiment and crystal plasticity simulation. Materials 13, 3069.
Mánik, T., Holmedal, B., Hopperstad, O.S., 2015. Strain-path change induced transients in flow stress, work hardening and -values in aluminum. Int. J. Plast. 69, 1–20.
Mott, N.F., 1952. A theory of work-hardening of metal crystals. Philos. Mag. A 43, 1151–1178.
Naghdi, P.M., Rowley, J.C., 1954. An experimental study of biaxial stress-strain relations in plasticity. J. Mech. Phys. Solid. 3, 63–80.
Pan, J., Rice, J.R., 1983. Rate sensitivity of plastic-flow and implications for yield-surface vertices. Int. J. Solid Struct. 19, 973–987.
Peeters, B., Seefeldt, M., Teodosiu, C., Kalidindi, S.R., Van Houtte, P., Aernoudt, E., 2001. Work-hardening/softening behaviour of BCC polycrystals during changing strain paths: I. An integrated model based on substructure and texture evolution, and its prediction of the stress-strain behaviour of an if steel during two-stage strain paths. Acta Mater. 49, 1607–1619.
Phillips, A., Lee, C.-W., 1979. Yield surfaces and loading surfaces. Experiments and recommendations. Int. J. Solid Struct. 15, 715–729.
Phillips, A., Moon, H., 1977. An experimental investigation concerning yield surfaces and loading surfaces. Acta Mech. 27, 91–102.
Phillips, A., Ricciuti, M., 1976. Fundamental experiments in plasticity and creep of aluminum—extension of previous results. Int. J. Solid Struct. 12, 159–171.
Radi, M., Abdul-Latif, A., 2012. A self-consistent approach describing the strain induced anisotropy: case of yield surface evolution. Comput. Mater. Sci. 54, 356–369.
Rauch, E.F., Gracio, J.J., Barlat, F., 2007. Work-hardening model for polycrystalline metals under strain reversal at large strains. Acta Mater. 55, 2939–2948.
Reyne, B., Barlat, F., 2022. A new concept for continuum distortional plasticity. Int. J. Plast. 155, 103303.
Roters, F., Diehl, M., Shanthraj, P., Eisenlohr, P., Reuber, C., Wong, S.L., Maiti, T., Ebrahimi, A., Hochrainer, T., Fabritius, H.-O., 2019. DAMASK–The Düsseldorf

Advanced Material Simulation Kit for modeling multi-physics crystal plasticity, thermal, and damage phenomena from the single crystal up to the component scale. Comput. Mater. Sci. 158, 420–478.
Schurig, M., Bertram, A., Petryk, H., 2007. Micromechanical analysis of the development of a yield vertex in polycrystal plasticity. Acta Mech. 194, 141–158.
Sharma, R., Sargeant, D., Daroju, S., Knezevic, M., Miles, M.P., Fullwood, D.T., 2022. Multi-strain path deformation behavior of AA6016-T4: experiments and crystal plasticity modeling. Int. J. Solid Struct. 244–245, 111536.
Simo, J.C., 1987. A J2-flow theory exhibiting a corner-like effect and suitable for large-scale computation. Comput. Methods Appl. Math. 62, 169–194.
Själander, M., Jahre, M., Tufte, G., Reissmann, N., 2019. EPIC: an Energy-Efficient, High-Performance GPGPU Computing Research Infrastructure arXiv preprint arXiv: 1912.05848.
Storen, S., Rice, J.R., 1975. Localized necking in thin sheets. J. Mech. Phys. Solid. 23, 421–441.
Toth, L.S., Molinari, A., Zouhal, N., 2000. Cyclic plasticity phenomena as predicted by polycrystal plasticity. Mech. Mater. 32, 99–113.
Van Dokkum, J.S., Bos, C., Offerman, B., Sietsma, J., 2021. Influence of dislocations on the apparent elastic constants in single metallic crystallites: an analytical approach. Materialia 20, 101178.
Wagoner, R.H., Lim, H., Lee, M.G., 2013. Advanced issues in springback. Int. J. Plast. 45, 3–20.
Wollmershauser, J., Clausen, B., Agnew, S., 2012. A slip system-based kinematic hardening model application to in situ neutron diffraction of cyclic deformation of austenitic stainless steel. Int. J. Fatig. 36, 181–193.
Wulfinghoff, S., Forest, S., Böhlke, T., 2015. Strain gradient plasticity modeling of the cyclic behavior of laminate microstructures. J. Mech. Phys. Solid. 79, 1–20.
Yoshida, K., 2017. A plastic flow rule representing corner effects predicted by rate-independent crystal plasticity. Int. J. Solid Struct. 120, 213–225.
Yoshida, K., Kuroda, M., 2012. Comparison of bifurcation and imperfection analyses of localized necking in rate-independent polycrystalline sheets. Int. J. Solid Struct. 49, 2073–2084.
Yoshida, K., Tsuchimoto, T., 2018. Plastic flow of thin-walled tubes under nonlinear tension-torsion loading paths and an improved pseudo-corner model. Int. J. Plast. 104, 214–229.
Zecevic, M., Knezevic, M., 2015. A dislocation density based elasto-plastic self-consistent model for the prediction of cyclic deformation: application to AA6022-T4. Int. J. Plast. 72, 200–217.
Zhang, K., Holmedal, B., Manik, T., Saai, A., 2019. Assessment of advanced Taylor models, the Taylor factor and yield-surface exponent for FCC metals. Int. J. Plast. 114, 144–160.
Zhang, T.Y., Han, X.H., 2023. Parameter identification for the non-associated flow rules representing corner effects through the equivalent tangential shear modulus reduction after abrupt strain-path change. Int. J. Plast. 169.
Zhang, T.Y., Liu, M.S., Han, X.H., 2022. A non-associated flow rule with simple non-branching form representing the apparent non-normality effects after abrupt strain-path change. Int. J. Plast. 159.